PCCP

ROYAL SOCIETY OF CHEMISTRY

PAPER

View Article Online
View Journal | View Issue

Cite this: *Phys. Chem. Chem. Phys.*, 2020, **22**, 2157

Self-assembly of MoO_3-decorated carbon nanofiber interlayers for high-performance lithium–sulfur batteries†

Huilan Li, Xiaofei Wang, Chu Qi, Chengcheng Zhao, Cuimei Fu, Lina Wang * and Tianxi Liu

Received 21st November 2019,
Accepted 20th December 2019

DOI: 10.1039/c9cp06287d

rsc.li/pccp

Lithium–sulfur (Li–S) batteries are attractive for next-generation energy storage systems due to their high theoretical capacity and energy density. However, the undesired shuttling of soluble lithium polysulfides (Li_2S_n, $2 < n \leq 8$) and the uncontrolled growth of lithium dendrites have hindered their practical applications. Herein, a self-assembled freestanding MoO_3/carbon nanofiber (MoO_3/CNF) composite membrane is effectively integrated into Li–S batteries as a functional interlayer. Improved cell performance is achieved due to the strong interfacial chemical and physical interactions between the interlayers with Li_2S_n. The Li–S batteries exhibit a decent cyclic stability with a fading rate of 0.12% per cycle for 500 cycles at 1675 mA g^{-1}, a high rate performance and a low self-discharge rate. In this rational design, the CNF network provides abundant electron pathways and physically prevents polysulfide diffusion. The polar MoO_3 nanorods act as effective anchoring sites by the chemical interactions with Li_2S_n. Meanwhile, the suppressed Li-dendrite growth on the Li-anode surface results in a stable Li stripping/plating.

Introduction

Lithium–sulfur (Li–S) batteries have been regarded as one of the most promising battery technologies due to their high energy density (2600 W h kg^{-1}), natural abundance and environmental friendliness of elemental sulfur (S_8).[1–3] However, some intractable issues have impeded the practical application of Li–S batteries. The major problem originates from the shuttle effect of soluble intermediate lithium polysulfides (Li_2S_n, $2 < n \leq 8$).[4–6] The use of the extremely reactive metallic Li anode and the dendrite growth on its surface are other challenges.[7,8] The notorious parasitic reactions between Li_2S_n and the Li metal lead to the severe loss of sulfur and the corrosion of the Li-metal surface. Nevertheless, in consideration of the intrinsic insulating nature of sulfur, the soluble Li_2S_n on the other side would facilitate a fast reaction kinetics. A way to tolerate the solubility of Li_2S_n but protect the Li-anode surface should be a reasonable solution for a high performance battery. Therefore, considerable efforts have been devoted to constructing a functional composite cathode to physically or chemically restrain polysulfide diffusion. Host/anchor materials of sulfur, including carbonaceous materials,[4,9] conductive polymers,[10,11] transitional-metal oxides,[9,12] sulfides,[13,14] and carbides,[15] have made significant progress.

Alternatively, incorporating a blocking interlayer between the separator and the sulfur cathode also provides a straightforward approach. The widely used micro-porous polypropylene (PP)/polyethylene (PE) separator is incapable of restraining polysulfide migration/diffusion due to a much larger pore size (<100 nm) than the dimension of polysulfide anions (<1 nm). Accordingly, Manthiram *et al.* assembled a microporous carbon interlayer between the cathode and the separator as a physical barrier to encapsulate Li_2S_n.[16] After that, various types of interlayers, including carbon nanotubes (CNTs),[17,18] carbon nanofibers,[19,20] graphene,[21,22] and other carbon-based materials,[23,24] have been proposed. However, the nonpolar surface of carbon materials makes it difficult to strongly anchor polar Li_2S_n to be well confined in the cathode side. Therefore, much attention has been paid to modifying the carbonaceous interlayer by polar inorganics, which can provide effective anchoring sites for Li_2S_n by chemisorption.[25–33] Xiao *et al.* coated the cathode with a TiO_2/graphene interlayer as an efficient polysulfide barrier.[25] Similarly, Kong *et al.* casted a MnO_2/graphene oxide/carbon nanotube[26] and Luo *et al.* casted a MoO_3/carbon nanotube interlayer[28] on the surface of the separator to alleviate the polysulfide shuttle effect. Owing to the synergistic effect of porous carbon and polar metal oxide additives, the composite interlayer acts as both a conductive network to facilitate electron conduction, and a chemical trapper to capture Li_2S_n.

State Key Laboratory for Modification of Chemical Fibers and Polymer Materials, College of Materials Science and Engineering, Innovation Center for Textile Science and Technology, Donghua University, Shanghai 201620, China.
E-mail: linawang@dhu.edu.cn

† Electronic supplementary information (ESI) available. See DOI: 10.1039/c9cp06287d

Nevertheless, such composite interlayers are generally made using a mixing-casting technology. The addition of polymer binders would inevitably reduce the overall battery energy density. And, up to now, limited attention has been paid to the effect of the interlayer on the Li-dendrite growth, the control of which is one of the most critical elements in the practical application of Li–S batteries. Therefore, it is crucial to construct a flexible composite interlayer with multi-functions through rational design.

Herein, we demonstrate a self-assembled freestanding MoO_3/carbon nanofiber (MoO_3/CNF) interlayer for Li–S batteries by combining the electrospinning technique and the solvothermal method. The interconnected CNF network provides fast charge transfer channels for the sulfur cathode and acts as a porous container to absorb Li_2S_n. Meanwhile, the MoO_3 nanorods serve as effective anchoring sites through strong chemical interactions with Li_2S_n. Benefiting from the synergetic effects, Li–S batteries exhibit a decent cyclic stability with a capacity decay of 0.12% per cycle for 500 cycles at 1C (1C = 1675 mA g^{-1}), a high rate performance and a low self-discharge rate. More importantly, the local growth of dendrites on the Li-metal surface is suppressed with the incorporation of the MoO_3/CNF interlayer, showing the broad potential for use in Li–S batteries.

Results and discussion

Preparation and structural analysis of MoO_3/CNF interlayers

Fig. 1 illustrates a schematic synthetic procedure for the freestanding MoO_3/CNF membranes. Firstly, a PAN precursor film was simply produced from a viscous solution of PAN/DMF by electrospinning, which is an efficient method for generating fibers with a stable freestanding architecture.[20,34] Subsequently, the PAN film was stabilized in air at 260 °C, followed by carbonization in Ar at 800 °C to prepare a CNF film. Finally, the self-assembled MoO_3/CNF membrane was obtained *via* a solvothermal method by directly immersing the CNF film into the precursor solution of MoO_3. During the solvothermal process, the MoO_3 was self-assembled onto the CNF film. MoO_3/CNF composite membranes with different MoO_3 contents were prepared, which were marked as MoO_3/CNF-1, MoO_3/CNF-2 and MoO_3/CNF-3, respectively.

Typically, the MoO_3/CNF-2 membrane exhibits a robust and flexible texture, as shown in Fig. 2a and b, which allows it to be readily bent or punched into a disc without apparent fractures. The field-emission scanning electron microscopy (SEM) images show that the PAN precursor film is composed of three-dimensional (3D) interconnected nanofibers (Fig. S1a, ESI†) with a uniform diameter

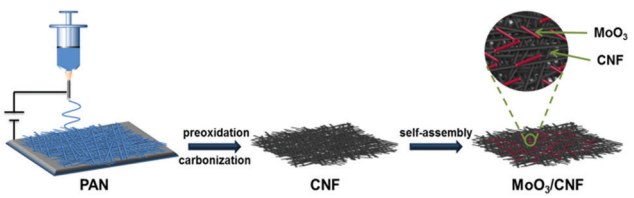

Fig. 1 Schematic illustration of the preparation of freestanding MoO_3/CNF membranes.

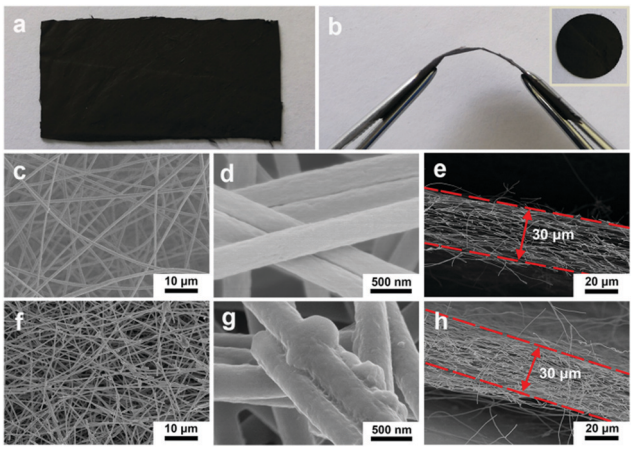

Fig. 2 (a and b) Optical images of the freestanding and flexible MoO_3/CNF-2 interlayer. SEM images of (c and d) CNF and (f and g) MoO_3/CNF-2. The cross-sectional images of (e) CNF and (h) MoO_3/CNF-2.

of 450 nm and rough surfaces (Fig. S1b, ESI†). After a heat-treatment process, the nanofibers of the CNF film show a smooth surface with a thinner diameter of ~250 nm (Fig. 2c and d). The average thickness of the CNF films is 30 μm (Fig. 2e). The overall view of MoO_3/CNF-2 reveals the homogenous self-assembled MoO_3 in the CNF network (Fig. 2f). The images with a higher magnification in Fig. 2g indicate that MoO_3 particles with a nanorod shape intertwine onto the carbon nanofibers. The overall thickness of MoO_3/CNF-2 is equivalent to that of the CNF film (Fig. 2h). Additional MoO_3/CNF membranes with different MoO_3 contents exhibit a similar 3D nanofibrous network with well self-assembled MoO_3 nanorods (Fig. S2, ESI†). The as-synthesized pure MoO_3 *via* the same hydrothermal reaction also shows a nanorod morphology (Fig. S3, ESI†).

The chemical composition and crystalline structure of MoO_3 powders, and CNF and MoO_3/CNF membranes were identified by X-ray diffraction (XRD) (Fig. 3a). The pattern of CNF exhibits a broad diffraction peak at 2θ = 26.5° corresponding to the graphitic (002) plane.[35,36] Besides the characteristic peak of the graphitized CNF, the MoO_3/CNF membranes exhibit several pronounced peaks that can be assigned to MoO_3 (JCPDS card no. 76-1003), coinciding with the pure MoO_3. In the Raman spectra (Fig. 3b), the MoO_3 exhibits several intensive peaks at 242, 290, 338, 380, 660, 818, and 998 cm^{-1}, indicating the high purity of α-MoO_3 crystals.[37] Both CNF and MoO_3/CNF show the two well-known D-band (disorder-induced phonon mode) at 1340 cm^{-1} and G-band (graphite band) at 1546 cm^{-1}. In comparison with CNF, MoO_3/CNF membranes show additional peaks at 100–1000 cm^{-1}, which are well in accordance with those of pure MoO_3. The thermogravimetry analysis (TGA) curves in Fig. 3c indicate that the content of MoO_3 in MoO_3/CNF-1, -2 and -3 is 12.5%, 19.0% and 23.7%, respectively.

Interactions between Li_2S_n and MoO_3 nanorods

The interaction between polysulfides and MoO_3 was verified by the adsorption experiment. Pure MoO_3 powders were added into an orange colored lithium polysulfide (Li_2S_6) solution

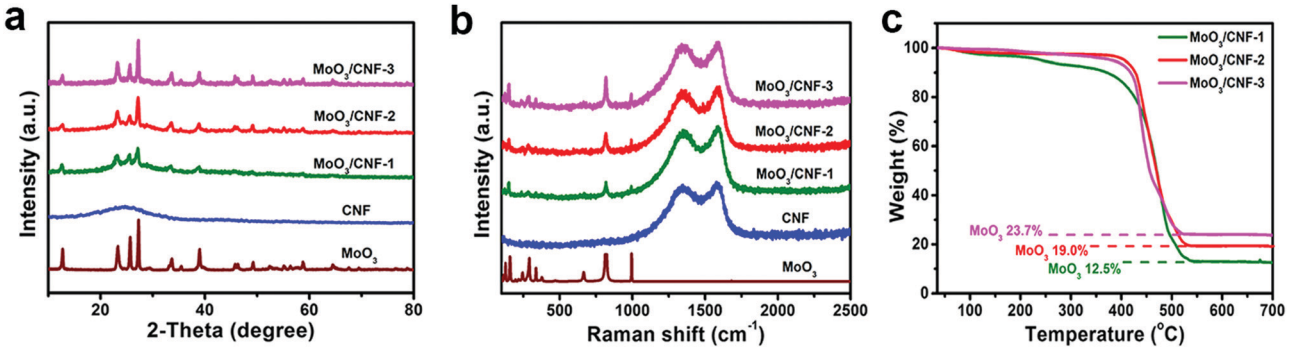

Fig. 3 (a) XRD patterns and (b) Raman spectra of as-prepared MoO_3, CNF and MoO_3/CNF. (c) TGA curves of MoO_3/CNF membranes with various contents of MoO_3 under an air atmosphere with a heating rate of 10 °C min^{-1}.

(5 mmol L^{-1}), which became nearly transparent (Fig. 4a inset photograph). The chemical states of the Li_2S_6 solution before and after adding MoO_3 were analyzed *via* UV-vis absorption spectroscopy (Fig. 4a). The characteristic peaks corresponding to S_8^{2-}/S_6^{2-} and S_6^{2-}/S_4^{2-} at 225 and 280 nm[25,38] decrease remarkably after the addition of MoO_3, suggesting the strong interaction between MoO_3 and polysulfides. X-ray photoelectron spectroscopy (XPS) provides the underlying adsorption principles. In the Mo 3d spectrum of pristine MoO_3, the doublets at 231.1 and 236.3 eV correspond to Mo $3d_{2/5}$ and Mo $3d_{2/3}$ of Mo^{6+},[28,39] and the weak peak at 231.5 eV is attributed to the presence of Mo^{5+} (Fig. 4b).[40] After soaking in Li_2S_6 solution, the two peaks assigned to Mo^{6+} slightly shift to lower binding energy, owing to the changed electron density of Mo^{6+} caused by the interaction with polysulfides.[28,40] It is noteworthy that the Mo^{5+} peak exhibits a stronger intensity, which could be ascribed to the reduction of Mo^{6+} by S_n^{2-}.[40] The S 2p spectrum of Li_2S_6-adsorbed MoO_3 can be deconvoluted into three species (Fig. 4c). The doublets observed at 163.0 and 164.6 eV are ascribed to the bridging and terminal sulfur atoms,[41,42] while the peak at 168.4 eV is assigned to a polythionate complex formed by the chemical reaction between MoO_3 and Li_2S_6.[42,43] The XPS analysis further confirms the chemical interaction between MoO_3 and polysulfides, which is helpful to suppress the polysulfide shuttle effect for an improved performance of Li–S batteries.

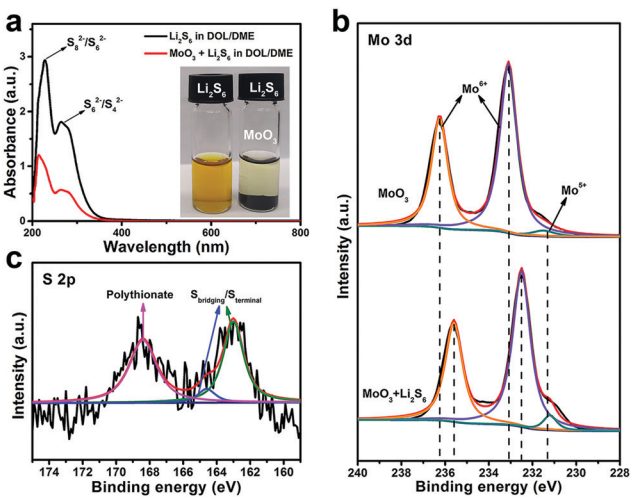

Fig. 4 (a) UV/vis absorption spectra and the digital images (the inset) of the Li_2S_6 solution before and after absorption by MoO_3. (b) Mo 3d spectra of MoO_3 before and after soaking in Li_2S_6 solution. (c) S 2p spectrum of Li_2S_6-adsorbed MoO_3.

Electrochemical performance of MoO_3/CNF interlayers

The self-assembled MoO_3/CNF is introduced as a freestanding interlayer between the cathode and the separator for Li–S batteries. The interlayer is expected to act as a selective filter that allows the free transport of electrolyte components while blocking the migration/diffusion of Li_2S_n, as shown by the schematic illustration in Fig. 5a. However, the battery performance is dependent on the content of MoO_3 in MoO_3/CNF. The galvanostatic cyclic test was performed within a potential window of 1.7–2.7 V. Compared to that using MoO_3/CNF-1 and MoO_3/CNF-3 interlayers, the cell with MoO_3/CNF-2 demonstrates a relatively lower voltage polarization (Fig. S4a, ESI†), higher cyclic performance (Fig. S4b and c, ESI†), and better rate performance (Fig. S4d, ESI†). The result suggests that less MoO_3 may not provide sufficient anchoring sites for Li_2S_n, whereas more MoO_3 would block the smooth charge pathways. Electrochemical impedance spectroscopy (EIS) of the fresh cells confirms the increased interfacial charge transfer resistance (R_{ct}) with the increasing content of MoO_3 (Fig. S4e, ESI†). Nonetheless, the cycled cell with MoO_3/CNF-1 shows the highest R_{ct} (Fig. S4f, ESI†), suggesting that polysulfide shuttling is not well controlled. The severe parasitic reactions between Li_2S_n and the Li anode would induce the degradation of the cathodic structure, corrosion and passivation of the Li-anode surface, leading to an increased R_{ct}.

The charge–discharge profiles of cells with or without interlayers exhibit the typical two major plateaus of Li–S batteries (Fig. 5b). Taking MoO_3/CNF-2, for example, the first discharge plateau at 2.3 V corresponds to the reduction step from S_8 to Li_2S_4, and the second plateau at 2.1 V is the further reversible reduction to Li_2S. A small sloped plateau at 1.72 V in the discharge profile reflects the irreversible reduction of $LiNO_3$ on the cathode.[44–46] The widely used $LiNO_3$-containing electrolyte was used in this work. The reduction of $LiNO_3$ on the

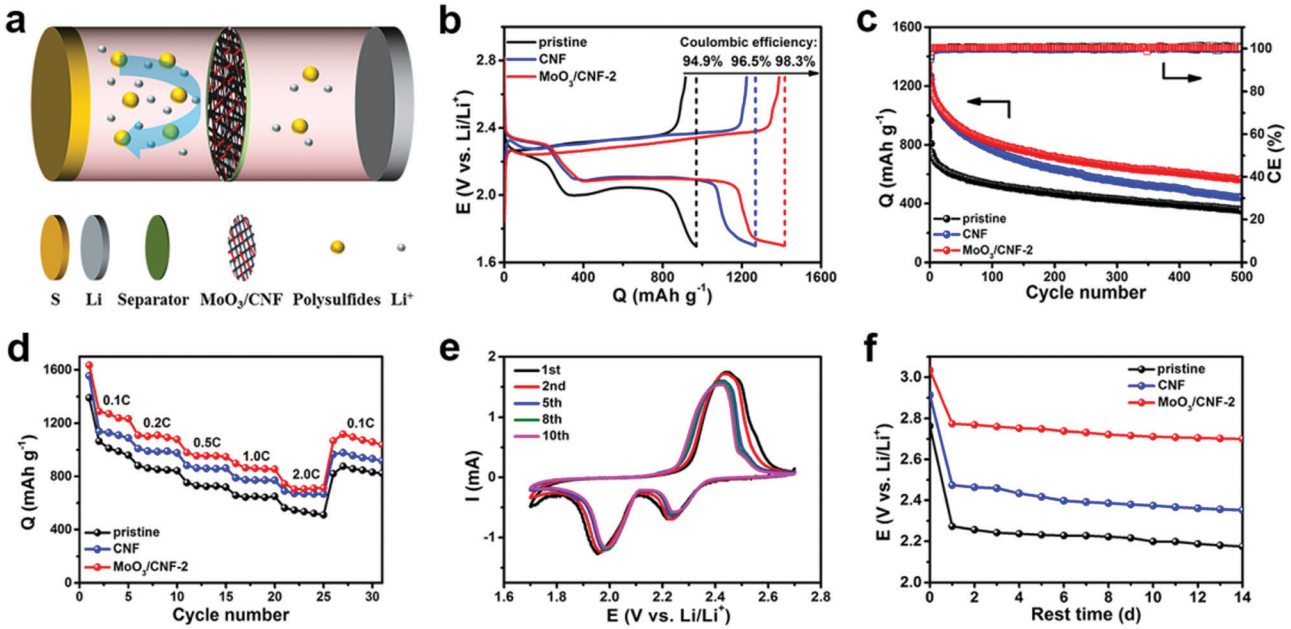

Fig. 5 (a) Schematic illustration of Li–S batteries with the MoO_3/CNF interlayer. (b) Initial galvanostatic discharge–charge profiles and (c) cycling performance of the cells without an interlayer, with a CNF or MoO_3/CNF-2 interlayer at 0.5C. (d) Rate capability test. (e) CV curves of cells with a MoO_3/CNF-2 interlayer at a scan rate of 0.1 mV s^{-1} for the initial 10 cycles. (f) Change in open-circuit voltages (OCVs) of the cells shelved for 14 days.

Li anode promotes the formation of a conductive solid–electrolyte interphase (SEI) layer, while that on the cathode adversely affects the reversibility and capacity of the Li–S battery. Under the current density of 0.5C, an initial CE of 98.3% is achieved for the cell with MoO_3/CNF-2, which is higher than those with the CNF interlayer (96.5%) and without the interlayer (94.9%). The initial discharge capacity of the cell without an interlayer is 965 mA h g^{-1}, while it reaches 1268 mA h g^{-1} for the cell with a CNF interlayer (Fig. 5c). However, the polysulfide shuttling is still severe with only a residual value of 440 mA h g^{-1} after 500 cycles. In contrast, the cell with MoO_3/CNF-2 delivers a higher initial discharge capacity of 1412 mA h g^{-1} and a better cyclic stability. The capacity fading rate is 0.11% per cycle after the 2nd cycle, indicating the suppressed redox shuttling of Li_2S_n. The long-term cycling at 1C also indicates an improved performance of the cell with MoO_3/CNF-2 (Fig. S5, ESI†).

The cell with the MoO_3/CNF-2 interlayer shows the highest capacity at various current densities from 0.1 to 2C (Fig. 5d). The specific capacity contributed by MoO_3/CNF-2 itself could be ruled out in the voltage of 1.7–2.7 V (Fig. S6, ESI†). The cyclic voltammetry (CV) plots of the cell with the MoO_3/CNF-2 interlayer for the initial 10 cycles are shown in Fig. 5e. Two main reduction peaks located at 2.23 and 1.96 V correspond to the conversion reaction of S_8 to Li_2S_4 and then to the final product of Li_2S, respectively. The peak at 2.42 V in the anodic scan along with a shoulder at 2.52 V is related to the reversible oxidation from Li_2S to Li_2S_4 and then to S_8. The somewhat overlap of the oxidative peaks indicates a fast reaction kinetics. No additional peaks can be seen in the CV curves, further implying that the interlayer is electrochemically inactive. The improved electrochemical performance should be attributed to the synergistic effects of the highly conductive carbon framework and strong anchoring ability of MoO_3. The self-discharge assessment provides more convincing evidence. The open-circuit voltages (OCVs) of the cells shelved for 14 days (d) are shown in Fig. 5f. The initial OCV of the fresh cell with the MoO_3/CNF-2 interlayer is 3.03 V, which is higher than those with CNF (2.91 V) and without an interlayer (2.84 V). After resting for 14 days, the OCV of the cell with CNF and without an interlayer finally decays to 2.35 and 2.17 V, respectively, implying the existence of self-discharge behavior.[22] In contrast, the cell with MoO_3/CNF-2 held a higher stabilized OCV in the following 14 days with a final cut-off voltage of 2.70 V, suggesting the inhibited self-discharge.

Protection of the Li anode by MoO_3/CNF interlayers

As is evident, the self-assembled MoO_3-decorated CNF interlayer is an efficient polysulfide immobilizer for Li–S batteries. The surface morphology of Li anodes after 500 galvanostatic cycles at 1C was examined by SEM characterization. Massive deposits are observed on the cycled Li anode without an interlayer (Fig. 6a). The Li-anode surface with a CNF interlayer is coarse with relatively regular deposits (Fig. 6b). By contrast, no obvious deposits could be seen on the Li-anode surface with the MoO_3/CNF-2 interlayer (Fig. 6c), indicating the suppressed corrosion of the Li anode derived from Li_2S_n. Insightful information on chemical/physical processes occurring at the electrode/electrolyte interface is available from the AC impedance measurements.[47] To understand the EIS results of the Li–S cells better, the relevant equivalent circuit models are provided (inset in Fig. 6d and e). And the EIS fitted parameters are also shown in Tables S1 and S2 (ESI†) for comparison. The EIS (Fig. 6d) suggests a similar R_{ct} of the fresh cells using MoO_3/CNF-2 (35.20 Ω) or CNF interlayers (35.86 Ω), which is lower than that without the interlayer (47.38 Ω). The cells after

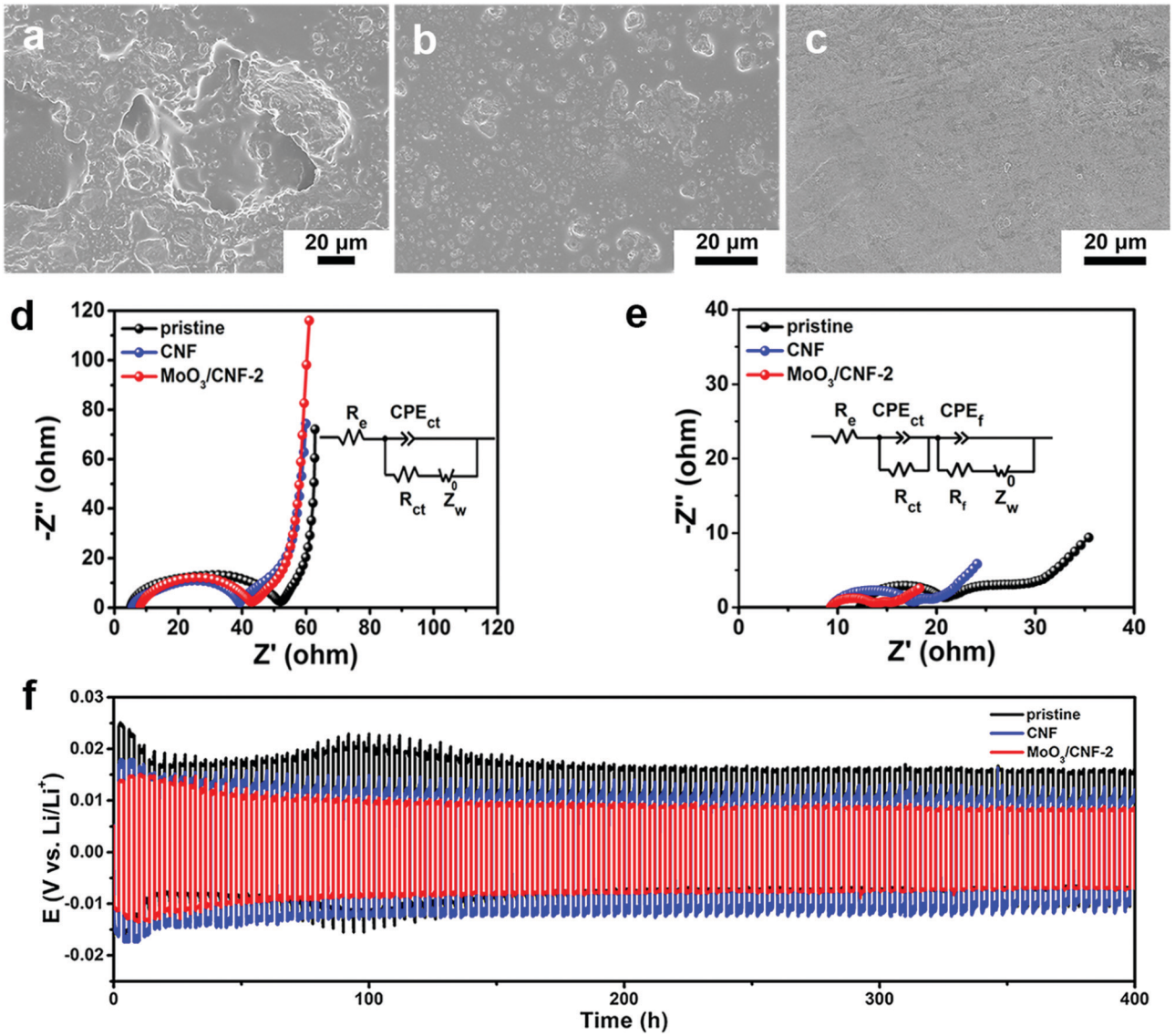

Fig. 6 SEM images of the Li-metal anode surface for the Li–S cells (a) without an interlayer, with a (b) CNF interlayer or (c) a MoO_3/CNF-2 interlayer after 500 cycles at 1C. EIS spectra of the Li–S cells (d) before and (e) after 500 cycles at 1C. The inset represents the corresponding equivalent circuit. (f) Voltage–time profiles of Li|Li symmetric cells at 0.5 mA cm^{-2} and 1 mA h cm^{-2}.

500 cycles show a general decreased total impedance. Compared with the insulating and solid S_8 cathode, the soluble and reactive properties of Li_2S_n would facilitate the reaction kinetics. Notably, the cycled cell with MoO_3/CNF-2 shows the lowest R_{ct} (4.68 Ω) and Li-diffusion resistance on the surface film (R_f, 4.17 Ω) (Fig. 6e), suggesting the reduced corrosion/passivation of the Li-anode surface. The reduced polysulfide shuttling has an impact on the suppression of Li-dendrite growth. The polysulfide shuttling can induce heterogeneities of the Li-metal surface because it causes passivation by bulk insulating Li_2S_2/Li_2S particles and electrolyte decomposition products. This promotes lithium dendrite formation and leads to poor lithium cycling efficiency with complicated Li-surface chemistry.[48–50]

We assembled symmetrical Li|Li cells to further investigate the effect of interlayers on Li-dendrite growth. The symmetrical cells were cycled at 0.5 mA cm^{-2} with a fixed capacity of 1 mA h cm^{-2} (Fig. 6f). The cell with the MoO_3/CNF-2 interlayer displays a superior cycling performance up to 400 h with a lower overpotential compared to the cell containing CNF, suggesting a stable Li stripping/plating process. In comparison, the overpotential of the cell without an interlayer increases rapidly after 70 h. This suggests that stable cycling does not occur since Ohm's law ($V = IR$) is not satisfied. EIS of the three Li|Li cells was also performed (Fig. S7a and b, ESI†). The relevant equivalent circuit model (Fig. S7c, ESI†) and the EIS fitted parameters (Tables S3 and S4, ESI†) provide more detailed information. Comparing the plots before and after cycling, all of the Li|Li symmetric cells show a decreased R_{ct} and R_f, and the cell with a MoO_3/CNF-2 interlayer exhibits the lowest total resistance. In terms of the Ohmic resistance of the electrolyte (R_e), the cycled cells with CNF or MoO_3/CNF-2 show reduced values compared with the respective fresh cells.

However, the cycled cell without an interlayer shows an increased R_e, which may result from the exfoliation of "dead Li" from the Li-metal surface due to the degradation at the interface. These results manifest the multi-functions of the self-assembled MoO_3-decorated CNF interlayer as an efficient polysulfide immobilizer and Li-metal stabilizer for advanced Li–S batteries.

Conclusions

In summary, a self-assembled MoO_3/CNF composite membrane was successfully integrated as a freestanding interlayer in Li–S batteries. The interlayer plays a crucial role in the improved cell performance through the immobilization of the sulfur cathode and stabilization of the Li-metal anode. In the MoO_3/CNF composite, the conductive CNF framework not only supplies an interconnected network for fast charge transfer but also acts as a physical barrier to resist Li_2S_n diffusion. Whereas, the polar MoO_3 nanorods further anchor the Li_2S_n through strong chemical interactions. Moreover, the reduced polysulfide shuttling would induce mitigated Li-dendrite growth on the Li-anode surface. Benefitting from these advantages, the Li–S cell delivers a high initial discharge capacity of 1412 mA h g^{-1} with a fading rate of 0.11% per cycle at 0.5C. Even at 2C, a specific capacity of 744 mA h g^{-1} can be reached, suggesting that the multifunctional interlayer is a promising candidate for high-performance Li–S batteries.

Experimental

Preparation of CNF and MoO_3/CNF interlayers

The CNF films were prepared *via* a simple electrospinning technology. Firstly, 0.5 g of polyacrylonitrile (PAN, M_w = 150 000, Sigma-Aldrich) was dissolved in 4.5 g of *N*,*N*-dimethylformamide (DMF, 99.5%, Shanghai Lingfeng Chemical) by vigorously stirring for 12 h. Subsequently, the mixture was electrospun onto the target rotating collector under optimized conditions with a feeding rate of 0.08 mm min^{-1}, an applied voltage of 15 kV and a tip-collector distance of 20 cm. After peeling off, the obtained PAN precursor films were annealed at 260 °C with a ramp rate of 1 °C min^{-1} for 1 h in air, followed by carbonizing at 800 °C for 2 h in argon with the heating rate of 5 °C min^{-1}. Finally, the self-assembled MoO_3/CNF interlayers were prepared by a hydrothermal reaction. In detail, 0.3 g of hexaammonium heptamolybdate tetrahydrate ($(NH_4)_6Mo_7O_{24}\cdot 4H_2O$, analytical purity, Sinopharm Chemical), 0.3 g of polyethylene–polypropylene glycol ($M_n \approx 5800$, Sinopharm Chemical) and 200 μL of hydrochloric acid (HCl, analytical purity, Sinopharm Chemical) were dissolved in 30 mL of deionized water by continuous stirring for 2 hours. The obtained solution was transferred into a Teflon-lined stainless-steel autoclave with 0.6, 0.3 and 0.2 g of CNF film immersed inside, respectively, and maintained at 180 °C for 24 h. Then, the films were taken out and rinsed with deionized water 3 times. After drying at 80 °C overnight under vacuum, MoO_3/CNF composite membranes with different MoO_3 contents were obtained, which were marked as MoO_3/CNF-1, MoO_3/CNF-2 and MoO_3/CNF-3, respectively. As a control, pure MoO_3 was synthesized by the same hydrothermal reaction except without adding the CNF film inside the solution.

Preparation of Li_2S_6 solution

The Li_2S_6 solution was prepared by reacting commercial Li_2S and sulfur (1 : 5 by mole ratio) in the mixed solvent of 1,3-dioxolane/1,2-dimethoxyethane (DOL/DME, 1 : 1 by volume) in an Ar-filled glove box.

Characterization

The morphologies of the pure MoO_3, PAN precursor film, CNF and MoO_3/CNF interlayers were attained *via* FESEM (S-4800, HITACHI). XRD (D/max-2550VB+/PC, Rigalcu) equipped with Cu-Kα radiation was used to characterize the structural properties. The content of MoO_3 in MoO_3/CNF was examined by TGA (NETZSCH TG 209 F1 Libra) in the temperature range of 25–800 °C under an air atmosphere. Raman spectra were collected by an inVia Reflex Raman Spectrometer (inVia-Reflex, Renishaw). UV-vis spectra were recorded by a UV-vis spectrophotometer (Lambda-35). XPS analyses were performed on a spectrometer (Escalab 250Xi) with Al Kα X-ray radiation.

Electrochemical measurements

A sulfur cathode (d = 12 mm), a sheet of CNF or MoO_3/CNF interlayer (d = 18 mm), a micro-porous separator (Celgard 2325, d = 18 mm) and a Li-anode (d = 14 mm) were assembled into a CR2025-type coin cell sequentially in an argon-filled glove box (<1 ppm of H_2O and O_2, Mikrouna). The cathode slurry was prepared from a mixture of the sublimed sulfur, Ketjenblack (KB) carbon powder and PVdF binder at a weight ratio of 60 : 30 : 10 in *N*-methy1-2-pyrrolidone (NMP). The as-prepared slurry was then casted on aluminum foil and dried at 50 °C overnight under vacuum. The cathodes were punched into discs with a diameter of 12 mm afterwards. 1 M lithium bis(trifluoromethanesulfone)imide (LiTFSI) in 1,3-dioxolane (DOL) and 1,2-dimethoxyethane (DME) (1/1, v/v) with a 0.2 M $LiNO_3$ additive were used as the electrolyte. The cells were evaluated under galvanostatic conditions using the LAND battery test system (Wuhan, China) in a voltage window of 1.7–2.7 V. CV was performed on an electrochemical workstation (Arbin Instruments, USA) at a scan rate of 0.1 mV s^{-1}. EIS measurements were conducted on a CHI660E electrochemical workstation in the frequency range of 100 kHz–0.1 Hz.

Conflicts of interest

There are no conflicts to declare.

Acknowledgements

The authors acknowledge financial support from the Natural Science Foundation of Shanghai (17ZR1446400), the Fundamental Research Funds for the Central Universities (2232018D3-02), the National Natural Science Foundation of China (21603030 and 51433001), the Program of Shanghai Academic Research

Leader (17XD1400100) and the Shanghai Scientific and Technological Innovation Project (18JC1410600).

Notes and references

1 A. Manthiram, Y. Fu, S.-H. Chung, C. Zhu and Y.-S. Su, *Chem. Rev.*, 2014, **114**, 11751.
2 Q. Pang, X. Liang, C. Y. Kwok and L. F. Nazar, *Nat. Energy*, 2016, **1**, 16132.
3 C. Zhao, H. Yang, X. Wang, H. Li, C. Qi, L. Wang and T. Liu, *Sustainable Energy Fuels*, 2019, **3**, 1966.
4 L. Wang, Y. Zhao, M. L. Thomas and H. Y. Byon, *Adv. Funct. Mater.*, 2014, **24**, 2248.
5 L. Wang, Y. Wang and Y. Xia, *Energy Environ. Sci.*, 2015, **8**, 1151.
6 L. Wang, X. Wang, J. Yuan, H. Yang, C. Fu, Y. Xia and T. Liu, *J. Mater. Chem. A*, 2018, **6**, 20737.
7 J. Wu, H. Zeng, X. Li, X. Xiang, Y. Liao, Z. Xue, Y. Ye and X. Xie, *Adv. Energy Mater.*, 2018, **8**, 1802430.
8 M. Yu, Z. Wang, Y. Wang, Y. Dong and J. Qiu, *Adv. Energy Mater.*, 2017, **7**, 1700018.
9 J. Wang, C. Fu, X. Wang, Y. Yao, M. Sun, L. Wang and T. Liu, *Electrochim. Acta*, 2018, **292**, 568.
10 S. Choudhury, P. Srimuk, K. Raju, A. Tolosa, S. Fleischmann, M. Zeiger, K. I. Ozoemema, L. Borchardt and V. Presser, *Sustainable Energy Fuels*, 2018, **2**, 133.
11 C. Xu, B. Xu, Y. Gu, Z. Xiong, J. Sun and X. S. Zhao, *Energy Environ. Sci.*, 2013, **6**, 1388.
12 Z. Li, J. Zhang and X. Lou, *Angew. Chem., Int. Ed.*, 2015, **54**, 12886.
13 Z. Yuan, H.-J. Peng, T.-Z. Hou, J.-Q. Huang, C.-M. Chen, D.-W. Wang, X.-B. Cheng, F. Wei and Q. Zhang, *Nano Lett.*, 2016, **16**, 519.
14 C. Ye, L. Zhang, C. Guo, D. Li, A. Vasileff, H. Wang and S.-Z. Qiao, *Adv. Funct. Mater.*, 2017, **27**, 1702524.
15 H.-J. Peng, G. Zhang, X. Chen, Z.-W. Zhang, W.-T. Xu, J.-Q. Huang and Q. Zhang, *Angew. Chem., Int. Ed.*, 2016, **55**, 12990.
16 S.-Y. Sheng and A. Manthiram, *Nat. Commun.*, 2012, **3**, 1166.
17 J.-Q. Huang, Z.-L. Xu, S. Abouali, M. A. Garakani and J.-K. Kim, *Carbon*, 2016, **99**, 624.
18 S.-Y. Sheng and A. Manthiram, *Chem. Commun.*, 2012, **28**, 8817.
19 Y. Yang, W. Sun, J. Zhang, X. Yue, Z. Wang and K. Sun, *Electrochim. Acta*, 2016, **209**, 691.
20 R. Singhal, S.-H. Chung, A. Manthiram and V. Kaira, *J. Mater. Chem. A*, 2015, **3**, 4530.
21 L. Zhang, F. Wan, X. Wang, H. Cao, X. Dai, Z. Niu, Y. Wang and J. Chen, *ACS Appl. Mater. Interfaces*, 2018, **10**, 5594.
22 J.-Q. Huang, T.-Z. Zhuang, Q. Zhang, H.-J. Hong, C.-M. Chen and F. Wei, *ACS Nano*, 2015, **9**, 3002.
23 N. Liu, B. Huang, W. Wang, H. Shao, C. Li, H. Zhang, A. Wang, K. Yuan and Y. Huang, *ACS Appl. Mater. Interfaces*, 2016, **8**, 16101.
24 Y. Fan, Z. Yang, W. Hua, D. Liu, T. Tao, M. M. Rahman, W. Lei, S. Huang and Y. Chen, *Adv. Energy Mater.*, 2017, **7**, 1602380.
25 Z. Xiao, Z. Yang, L. Wang, H. Nie, M. Zhang, Q. Lai, X. Xu, L. Zhang and S. Huang, *Adv. Mater.*, 2015, **27**, 2891.
26 W. Kong, L. Yan, Y. Luo, D. Wang, K. Jiang, Q. Li, S. Fan and J. Wang, *Adv. Funct. Mater.*, 2017, **27**, 1606663.
27 M. Liu, Q. Li, X. Qin, G. Liang, W. Han, D. Zhou, Y.-B. He, B. Li and F. Kang, *Small*, 2017, **13**, 1602539.
28 L. Luo, X. Qin, J. Wu, G. Liang, Q. Li, M. Liu, F. Kang, G. Chen and B. Li, *J. Mater. Chem. A*, 2016, **6**, 8612.
29 L. Tan, X. Li, Z. Wang, H. Guo and J. Wang, *ACS Appl. Mater. Interfaces*, 2018, **10**, 3707.
30 Z. A. Ghazi, X. He, A. M. Khattak, N. A. Khan, B. Liang, A. Lqbal, J. Wang, H. Sin, L. Li and Z. Tang, *Adv. Mater.*, 2017, **29**, 1606817.
31 J. Park, B.-C. Yu, J. S. Park, J. W. Choi, C. Kim, Y.-E. Sung and J. B. Goodenough, *Adv. Energy Mater.*, 2017, **7**, 1602567.
32 L. Wang, Y.-B. He, L. Shen, D. Lei, J. Ma, H. Ye, K. Shi, B. Li and F. Kang, *Nano Energy*, 2018, **50**, 367.
33 Y. Luo, N. Luo, W. Kong, H. Wu, K. Wang, S. Fan, W. Duan and J. Wang, *Small*, 2018, **14**, 1702853.
34 A. Greiner and J. H. Wendorff, *Angew. Chem., Int. Ed.*, 2007, **46**, 5670.
35 X. Zhu, W. Zhao, Y. Song, Q. Li, F. Ding, J. Sun, L. Zhang and Z. Liu, *Adv. Energy Mater.*, 2018, **8**, 1800201.
36 T. H. Hwang, D. S. Jung, J.-S. Kim, B. G. Kim and J. W. Choi, *Nano Lett.*, 2013, **13**, 4532.
37 L. Mai, B. Hu, W. Chen, Y. Qi, C. Lao, R. Yang, Y. Dai and Z. L. Wang, *Adv. Mater.*, 2007, **19**, 3712.
38 Y. Li, H. Zhan, S. Liu, K. Huang and Y. Zhou, *J. Power Sources*, 2010, **195**, 2945.
39 X.-Y. Yue, X.-L. Li, J.-K. Meng, X.-J. Wu and Y.-N. Zhou, *J. Power Sources*, 2018, **397**, 150.
40 S. Lmtiaz, Z. A. Zafar, R. Razaq, D. Sun, Y. Xin, Q. Li, Z. Zhang, L. Zheng, Y. Huang and J. A. Anderson, *Adv. Mater. Interfaces*, 2018, **5**, 1800243.
41 X. Wang, G. Li, J. Li, Y. Zhang, A. Wook, A. Yu and Z. Chen, *Energy Environ. Sci.*, 2016, **9**, 2533.
42 X. Liang, C. Hart, Q. Pang, A. Garsuch, T. Weiss and L. F. Nazar, *Nat. Commun.*, 2015, **6**, 5682.
43 X. Liang, C. Y. Kwok, F. Lodi-Marzano, Q. Pang, M. Cuisinier, H. Huang, C. J. Hart, D. Houtarde, K. Kaup, H. Sommer, T. Brezesinki, J. Janek and L. F. Nazar, *Adv. Energy Mater.*, 2016, **6**, 1501636.
44 Y. Mikhaylik and V. Yuriy, *US Pat.*, B2, 7354680, 2008.
45 S. S. Zhang, *J. Electrochem. Soc.*, 2012, **7**, A920.
46 S. S. Zhang, *Electrochim. Acta*, 2012, **70**, 344.
47 J. T. Irvine, D. C. Sinclair and A. R. West, *Adv. Mater.*, 1990, **2**(3), 132.
48 C. Zhu and A. Manthiram, *J. Phys. Chem. Lett.*, 2014, **5**, 2522.
49 S. H. Kim, J. S. Yeon, R. Kim, K. M. Choi and H. S. Park, *J. Mater. Chem. A*, 2018, **6**, 24971.
50 X. Ni, T. Qian, X. Liu, N. Xu, J. Liu and C. Yan, *Adv. Funct. Mater.*, 2018, **28**, 1706513.